Supplementary Information

Interdiffusion control in sequentially evaporated organic-inorganic perovskite solar cells

Rahul A. Nambiar[1], David P. Mcmeekin[1], Manuel Kober Czenry[1], Joel A. Smith[1], Margherita Taddei[3], Pietro Caprioglio[1], Amit Kumar[1], Benjamin W. Putland[1], Junke Wang[1], Karim A. Elmestekawy[1], Akash Dasgupta[1,] Seongrok Seo[1], Jin Yao[2], Grey Christophoro[1], Daniel J Graham[4], Laura M Herz[1], David Ginger[3], Henry J. Snaith[1] *.

[1]Department of Physics, University of Oxford, Clarendon Laboratory, Parks Road, Oxford OX1 3PU, United Kingdom
[2] EPSRC National Thin Film Facility for Advanced Functional Materials (NTCF), Department of Physics, University of Oxford, United Kingdom.
[3]Department of Chemistry, University of Washington, Box 351700, Seattle, Washington 98195-1700, United States.
[4]Department of Bioengineering, University of Washington, Seattle, Washington 98195

Experimental Methods

Materials

Lead iodide PbI_2(99.998 metal base, ultra-dry), cesium iodide CsI (99.998% metal base, ultra-dry), lead chloride $PbCl_2$ (99.998% metal base) and bathocuproine BCP was purchased from Alfa Aeser, $CH(NH_2)_2$ formamidinium iodide was purchased from Dyenamo and vacuum dried overnight at 80 °C before being brought into the vacuum chamber. Spiro-TTB (98%) was purchased from Lumtec. C60 fullerene (99.999 thrice sublimed) was purchased from CreaPhys. Indium tin oxide-coated glass substrates (ITO, 15 Ω cm-2, AMG) were purchased from biotan. Silver pellets (Ag, 99.999%), gold pellets (Au, 99.999%) and Chromium (bar) were purchased from Kurt J. Lesker company. ALD tin oxide precursor TDMASn was purchased from Pegasus Chemicals. SiOx sputter target (99.99%) was purchased from Angstrom Engineering Inc.

Solar cell fabrication

ITO glass substrates were cleaned using industrial detergent Decon90 (1ml solution in de-ionised water) followed by acetone and isopropanol. The glass substrates are then placed under UV-Ozone for 20 minutes.

Glass substrates are then brought into a Nitrogen filled glovebox and loaded onto an Angstrom thin-film cluster which consists of a high vacuum designed (10^{-8} mbar) load lock connected to five physical vapor deposition system tools through two handling units. In the p-i-n stack the hole transport layer, 5nm of Spiro-TTB is deposited in the first thermal evaporated at 10^{-8}mbar at 0.2 Å/s. The substrates are then transferred under 10^{-8} mbar to the perovskite chamber without breaking vacuum. For the perovskite layer, Inorganic precursors specifically 250nm lead iodide, cesium iodide and lead chloride are first co-evaporated under 10^{-7}mbar pressure at 0.9 Å/s, 0.132 Å/s and 0.15 Å/s respectively with respect to lead iodide as explained in our previous work by Lohmann et al[1]. After depositing of inorganic precursors, multi-source 248nm of formamidium iodide is evaporated from 2 individual sources at a cumulative rate of 0.5 Å/s keeping individual sources below 180°C to prevent substantial formation of sym-triazine. During the deposition of formamidinium iodide the vacuum chamber pressure increases to 10^{-6}mbar which is expected during the sublimation of organo halides. The ITO/Spiro-TTB/Perovskite half-stacks are then brought out of vacuum and placed into a dry box with meticulously controlled (the sensor error is within ± 3%) 35%RH and annealed at 150°C for 20 minutes The time that it is outside of the glovebox before annealing is approximately 2 minutes while loading on to the hot plate. Post annealing, the substrates are loaded back into the load lock for n-type contacts. 20 nm of C60 fullerene followed by 5nm BCP and 120 nm Ag are evaporated at the rate of 0.2 Å/s, 0.1 Å/s and 1 Å/ respectively. For cells used for accelerated aging, BCP is replaced with 20 nm ALD tin oxide. Stable metal contacts thermally evaporated 3.5 nm chromium and 80 nm Gold are evaporated under 10^{-6}mbar at the rate of 0.05 Å/s and 1 Å/s respectively, followed by 300 nm sputtered silicon dioxide at 0.3 Å/s under 10^{-3}mbar.

Scanning Electron Microscopy (SEM)

Top-down SEM and cross section micrograms were taken on an FEI Quanta 600 FEG at an accelerating voltage of 5 kV. The SEM chamber was pumped down to high vacuum of < 2 × 10-4 mbar.

Ultraviolet Absorption

The UV-Vis absorption spectra were measured between 400-850 nm using a Fourier transform infrared (FTIR) spectrometer Cary 5000.

X-ray Diffraction

XRD measurements were performed using a Panalytical X'Pert Pro with Cu Kα1 X-ray source (λ=1.5406 Å) in ambient air.

Grazing incidence wide angle x ray scattering

GIWAXS data was acquired at the I07 beamline at Diamond Light Source. Samples were fabricated following the above procedure and transferred (sealed in N_2) to the synchrotron and measured the following day. Samples were loaded on to a hot plate either into an N_2-flushed chamber or measured in ambient air (30-40% RH), with air exposure only during loading for N_2-annealed samples. X-rays with energy 10 keV were incident on the samples at a grazing incidence angle (α_i) of 2° during continuous in-situ measurement for 15 minutes. Samples were annealed at a setpoint of 150 °C (reached at 120 s) which was measured through a PID controller and independently at the hotplate surface. Damage due to the incident beam was avoided by using appropriate beam attenuation. Scattering from the sample was collected by a Pilatus 2M (DECTRIS) hybrid photon-counting detector with a sample-to-detector distance (SDD) of 375 mm, with the geometry calibrated using LaB_6. Additional in situ GIWAXS data was acquired with a lab-based SmartLab (RIGAKU) diffractometer with a 3 kW Cu X-ray source (8.04 keV) combined with a DCS-350 heating stage (ANTON-PAAR). For these measurements, samples were transferred directly from the glovebox and measured in air with no extended ambient exposure, and the hotplate was set to 150 °C immediately (at the start of measurement). The SmartLab was operated in parallel beam configuration with 0.5° pinhole optics, a 1° in-plane parallel slit collimator, and 0.3° long collimator attachments. Scattering was collected with a HyPix-3000 (RIGAKU) 2D detector with 110 mm SDD at α_i = 3° and with the detector goniometer arm at a rotation of 14°. For each measurement, the acquisition time was 15 s. Data reduction in all cases, including remapping detector images into Q-space and in situ plotting, were performed using scripts based on the PyFAI and pygix libraries.[2, 3]

Time of Flight Secondary ion mass spectroscopy

Positive and negative ion ToF-SIMS depth profiles were acquired using an IONTOF ToF-SIMS 5 spectrometer. Profiles were acquired in the non-interlaced mode. Spectra/images were acquired using a 25 keV Bi_3^+ cluster ion source in the pulsed mode using delayed extraction mode. Data was acquired using a 100-micron x 100-micron spot at 256 x 256 pixels. The ion source was operated with a current of 0.02 pA to avoid saturation in the spectra. The primary ion dose per layer was $1.1x10^{11}$ ions/cm^2. Sputtering was done using a gas cluster ion source using 20keV argon 1000 clusters with a current of 6.96 nA over an area of 500-micron x 500 micron. The sputter dose per layer was $5x10^{13}$ ions/cm^2. An electron flood gun and argon flooding were also used for charge neutralization. Positive ion data were calibrated using the Cs^+, Pb^+ and $Cs2I^+$ peaks with calibration errors less than 40 ppm. Negative ion data were calibrated using the Br^-, I^-, $PbI2^-$ and $PbI3^-$ peaks with calibration errors less than 25 ppm. Mass resolution (m/Δm) for positive ion data was ~5500 for m/z = 133 (Cs^+). Mass resolution (m/Δm) for negative ion data was ~4700 for m/z = 127 (I^-).

Photoluminescence Quantum Efficiency Measurement

Photoluminescence quantum efficiency measurements were acquired using a custom built PLQE setup in an integrating sphere. Samples were photoexcited using a 532 nm laser (laser power = 0.585 mW). The PL was collected using a high-resolution monochromator and hybrid photomultiplier detector assembly (PMA Hybrid 40, Pico Quant GmbH). The PLQE were extracted from the photon energy (hf), photon numbers of the excitation and emission obtained from numerical integration using Python.

Time-resolved photoluminescence

TRPL of the Spiro-TTB/Perovskite half-stacks was measured using TCSPC (time-correlated single photon counting) with a FluoTime300 (Picoquant). The samples were excited with a 532 nm picosecond pulsed diode laser at a repetition rate of 0.1 MHz (LDH-P-C-510, Picoquant). The maximum fluence of the laser was 3.8 x 10^{10} cm^{-2}. The emitted PL was collected and coupled into PMT detector (dead time < 95 ps), which was coupled to a single photon counting electronics (TimeHarp260 nano, Picoquant). The TCSPC method assumes that all photons observed by the detector are single photons. To make sure that this is the case, the pile-up rate, which is defined as the ratio of the rate of emission to the rate of excitation, should be low. This reduces the probability of two photons arriving at the detector simultaneously. Hence, for all measurements done in this work, we kept the pile-up rate below 5%.

PHYSICAL MODEL

For each of the Spiro-TTB/Perovskite half-stack samples, we measured the TRPL for two excitation intensities (3.8×10^{10} cm^{-2} and 3.8×10^{9} cm^{-2}) from both the Spiro-TTB and air side. Then a set of these four measurements is co-assessed with a recently reported method[4], where we Bayesian inference together with a full physical model to discern the influence of 7 device-relevant parameters on the observed TRPL data. In short, we calculate the TRPL curves based on a set of parameter values that is selected by a Markov-chain Monte-Carlo (MCMC) algorithm and estimate the likelihood that the calculation matches the data using Bayes' theorem. After 10k steps of the MCMC chain we then get histograms for each parameter shown in **Fig. S(12-S15)** respectively, which show how many times each value of a given parameter was sampled. With this approach, we are able to distinguish between the recombination at the Spiro-TTB/Perovskite (S_{bot}) and the Perovskite/air (S_{top}) interface, as well as the vertical charge carrier mobility (μ_{vert}), and the non-radiative bulk recombination ($k_{\text{nr, bulk}}$). The results are shown in Figure 3C. in the main text, as well as **Fig. S(12-15)** in the supporting information.

There are more parameters that are obtained, but they are either non-identifiable (their values span multiple orders of magnitude) or they are comparable between the different samples and hence not crucial for this work. We still report all histograms in **(Fig. S12-S15)** to allow the reader to draw their own conclusions from this data.

Optical Pump Terahertz Probe (OPTP) Spectroscopy

An amplified laser system (Spectra Physics, MaiTai – Ascend – Spitfire), with a 5 kHz repetition rate, centre wavelength of 800 nm and pulse duration of 35 fs is used to generate the THz radiation using a spintronic emitter. The THz probe is then focused onto the sample, overlaid with a 400 nm excitation pump that is generated using a Beta Barium Borate (BBO) crystal. The THz radiation transmitted through the sample is then detected via free-space electro-optical sampling in a ZnTe (110) crystal of thickness 200 µm.

OPTP spectroscopy allows us to non-invasively probe the dielectric response of a medium and examine the charge carriers that modify the material's conductivity at THz frequencies after a well-defined time delay after optical excitation. This approach allows us to investigate the local charge-carrier dynamics and quantify the effective mobilities and bimolecular recombination rates of the photogenerated charge carriers.

Charge-carrier sum mobility:

Time-resolved variations in the THz transmission ($\Delta T/T$) through the sample can be measured by varying the time delay between the pump and probe beams, and this change in electric field transmission at the peak of the THz pulse (t_{gate}) can be in turn related to the change in the photoconductivity (ΔS) of the thin film (films whose thickness d is much smaller than the THz wavelengths λ_{THz}), using:

$$\Delta S = -\epsilon_0 c(n_a + n_b)\frac{\Delta T(t_{gate} = 0)}{T},$$

where $\epsilon_0 c$ is the invert of the vacuum impedance, and n_a and n_b are the refractive indices of the mediums surrounding the sample (vacuum and the substrate). The charge-carrier mobility (μ) and change in photoconductivity (ΔS) have a linear relationship that holds for low fluences (< 50 $\mu J\ cm^{-2}$), described using:

$$\mu = \frac{\Delta S A_{eff}}{Ne},$$

where A_{eff} is the effective area of overlap between the optical pump and the THz probe, and N is the number of photoexcited charge carriers.

The number of photoexcited charge carriers can be calculated using:

$$N = \Phi E\lambda\, hc\left(1 - R_{pump} - T_{pump}\right),$$

where Φ is the branching ratio of free charge-carriers to photons absorbed, $\left(1 - R_{pump} - T_{pump}\right)$ is the fraction of the 400 nm pump beam absorbed by the sample, λ and E are the wavelength and pulse energy of the excitation pulse, and $E\lambda\, hc = N_{ph}$ is the number of photons in a pump pulse.

We can then combine these equations to calculate the effective charge-carrier mobility as:

$$\Phi\mu = -\epsilon_0 c\left(n_a + n_b\right)\frac{A_{eff}\,hc}{Ee\lambda\left(1 - R_{pump} - T_{pump}\right)}\left(\frac{\Delta T\left(t_{gate}, t_{pump-probe} = 0\right)}{T}\right).$$

This effective mobility is the effective sum mobility of photogenerated electrons and holes, and it reflects the true sum mobility when the photons absorbed are fully converted to free charge carriers (Φ = 1)

External Quantum Efficiency

External quantum efficiency (EQE) measurements were performed using a custom built set up based on a Bruker Vertex 80v Fourier transform interferometer. The solar cells were illuminated with a 250 W quartz-tungsten halogen lamp that was first passed through a monochromator (Princeton Instruments SP2150) with a filter wheel (Princeton Instruments FA2448), then chopped with an optical chopper (Thorlabs MC2000B) at 280Hz, and finally focussed onto the sample with a smaller spot size than the solar cell area (as defined by the metallic top contact). The amplitude of the resulting AC current signal was measured with a lock-in amplifier (Stanford Research Systems SR830) as the voltage drop across a 50 Ohm resistor in series with the solar cell. To determine the EQE, the photocurrent spectrum of the device under test was divided by that of a calibrated Si reference cell (Thorlabs FDS100-CAL) of a known EQE. Device active areas were masked with a black-anodised metal aperture, having an active area of 0.25 cm2.

Solar cell characterisation and stability test

Current-voltage and maximum power point measurements were measured using two Keithley 2400 series source meters in the ambient environment under both simulated sunlight (AM 1.5 irradiance generated by a Wavelabs SINUS-220 simulator) and in the dark. The active area of the solar cell was masked with a black-anodized metal aperture to either 0.25cm^2, within a lighttight holder. The current-voltage characteristics were taken from a "reverse" scan (i.e., from "forward bias" to active maximum power point tracking measurements using a gradient descent algorithm were performed for 30 seconds to obtain the maximum power point tracked efficiency. The intensity of the solar simulator was set periodically such that the short-circuit current density from a KG3-filtered Si reference photodiode (Fraunhofer ISE) matched its 1-sun certified value. A local measurement of the intensity before each batch of solar cell measurements were performed, was made by integrating the spectrum obtained from the solar simulator's internal spectrometer. By taking the ratio of this internal intensity measurement to one obtained at the time of calibration we determined the equivalent irradiance at the time of measurement. The mismatch factor estimated for the test cells, calibration cells and simulator were estimated to be less than 1% and was hence not applied.

The perovskite solar cells were encapsulated using a cover glass (28.0 mm × 21.5 mm × 1.1 mm for the glass and 25 mm × 18.5 mm × 0.5 mm for the cavity, AMG) and UV adhesive (LT-U001, Lumtec) in a nitrogen-filled glovebox. All the encapsulated devices were aged using an Atlas SUNTEST CPS+ (1,500 W air-cooled Xenon lamp) light soaking chamber under simulated full-spectrum AM1.5 sunlight with ~ 77 mW cm-2 irradiance and without applying any UV filters. All the aging tests performed in this work were conducted in open-circuit conditions. To carry out current-voltage characterizations, the samples were taken out from the chamber and tested at different ageing times, following the measurement protocol as described above. The ageing chamber for storing the encapsulated samples was air-cooled with the temperature controlled at 85 ℃ (measured using a black standard temperature control unit positioned next to the test cells). During the ageing period, the relative humidity in the laboratory (at ~ 21°C) was monitored in the range of 50 ~ 60%.

Supplementary figures:

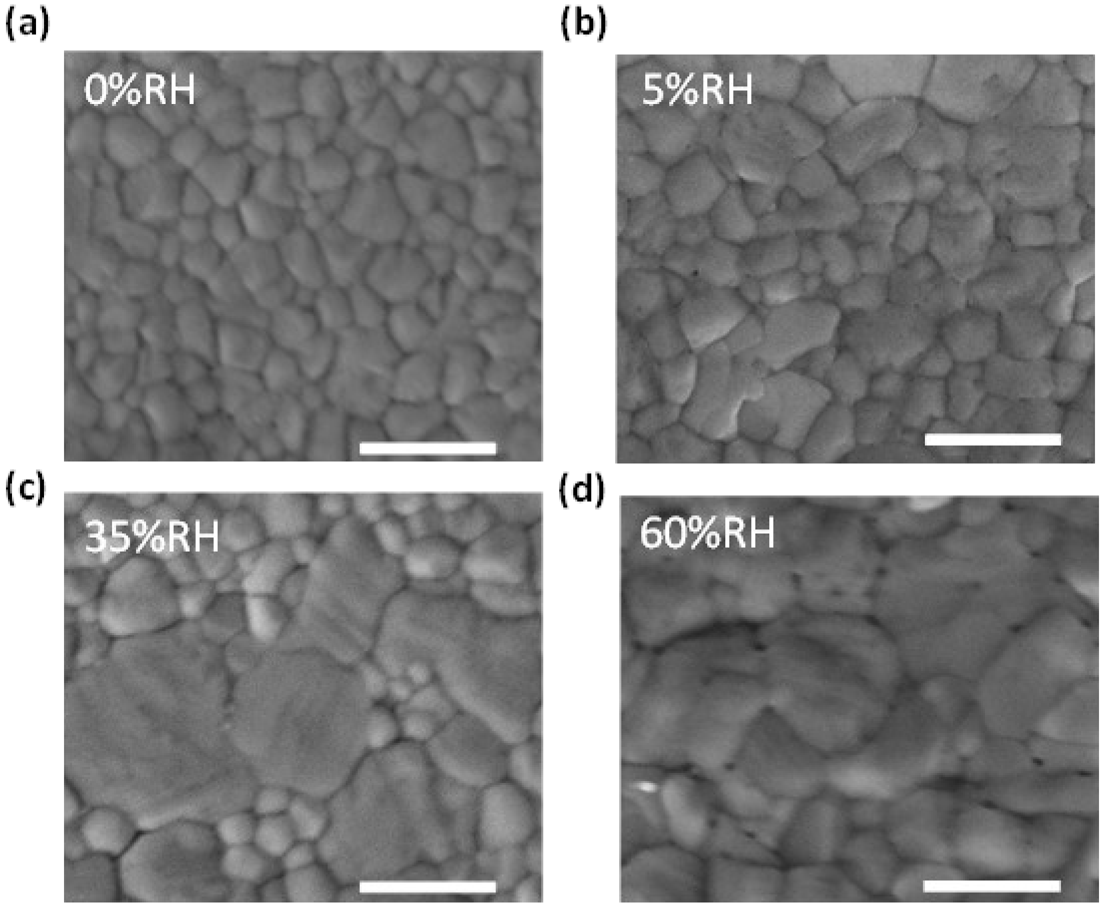

Supplementary Figure 1: Top view scanning electron micrograms (SEM) of sequentially evaporated films annealed under 0%, 5%, 35% and 60%RH. Scale bar is 1 micron

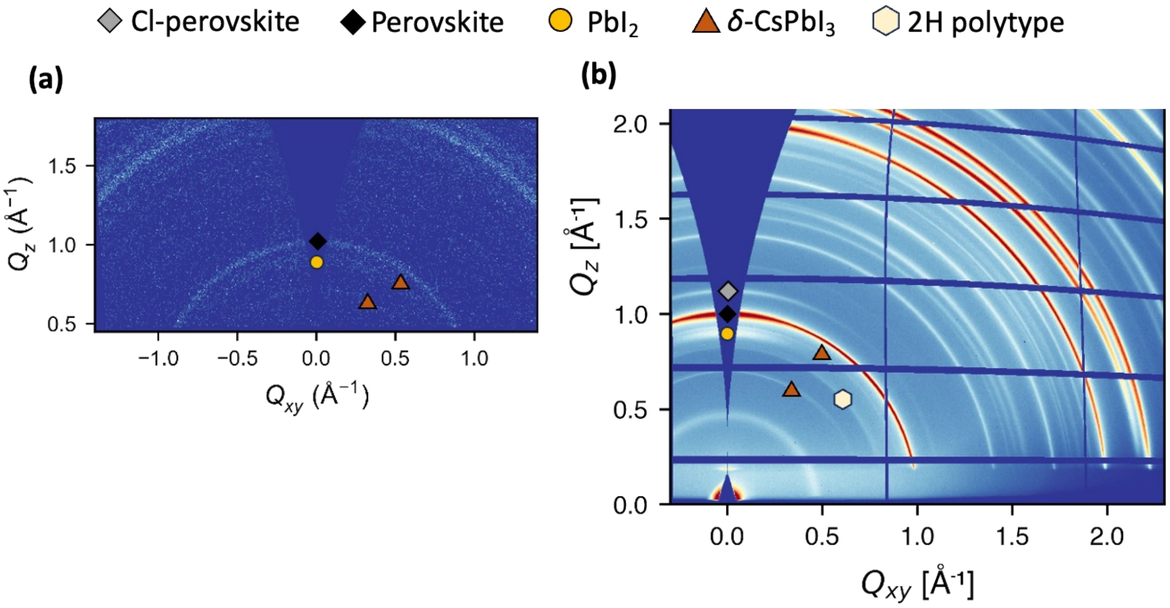

Supplementary Figure 2: Grazing incidence wide-angle X ray scattering (GIWAXS) of sequentially evaporated precursor stage films obtained using a) in house and b) synchrotron measurements respectively.

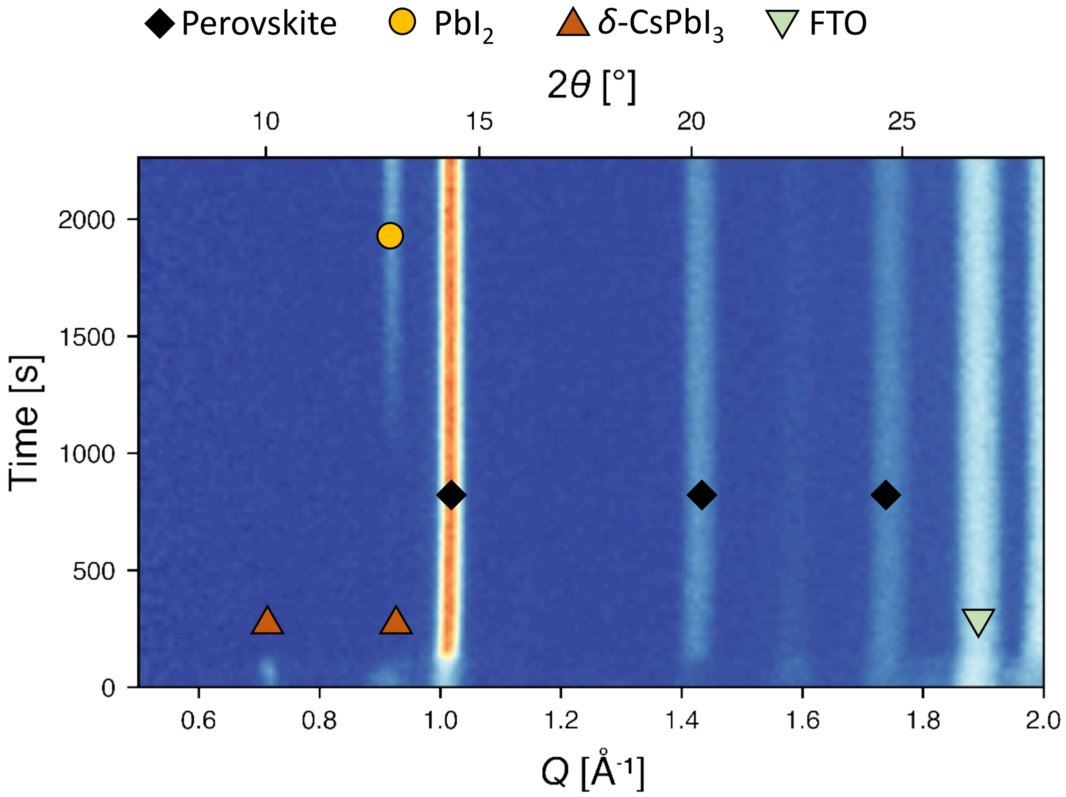

Supplementary Figure 3: In-situ grazing incidence wide angle X ray scattering (GIWAXS) of a sequentially evaporated perovskite film during annealing using lab-based measurements.

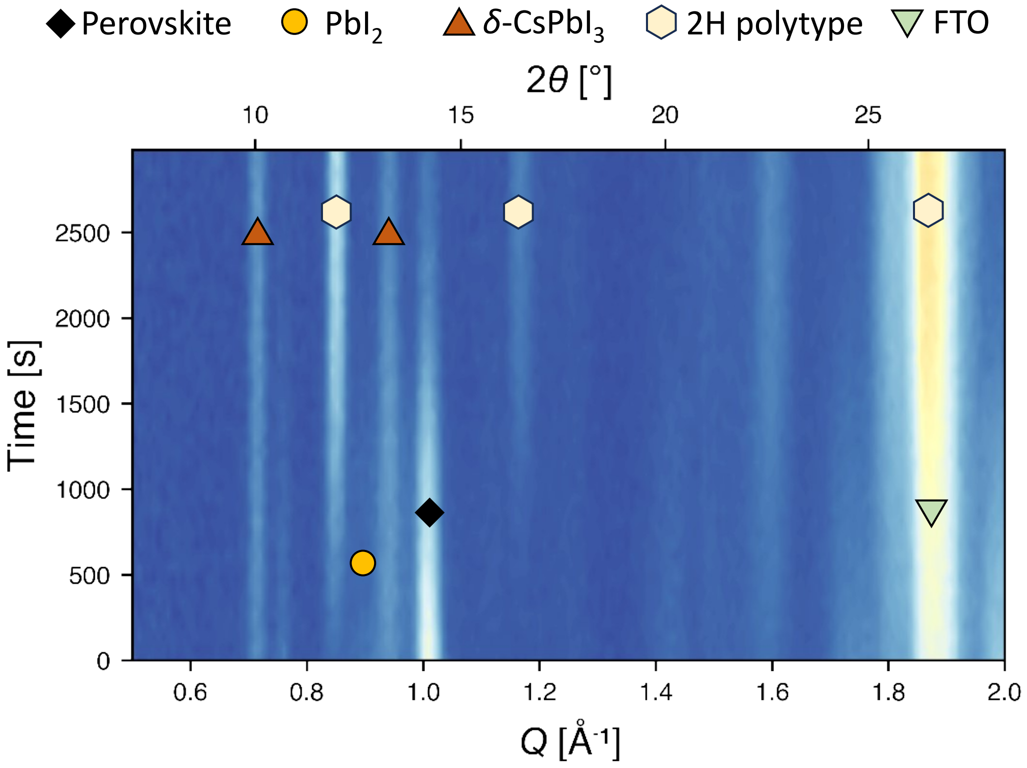

Supplementary Figure 4*:* In-situ grazing incidence wide angle X ray scattering (GIWAXS) of a sequentially evaporated perovskite precursor film when it is allowed to rest under the presence of controlled in ambient air with a relative humidity (30-40% RH) at room temperature in air.

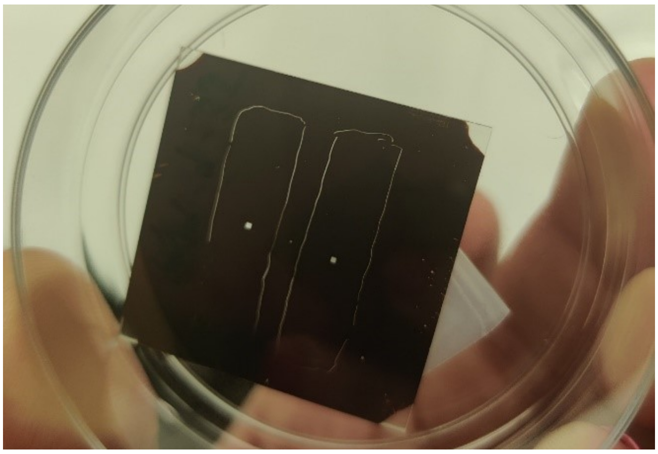

Supplementary Figure 5: 100x100 micron spots where ToF SIMS was conducted on a sample for +ve and -ve charged ions respectively

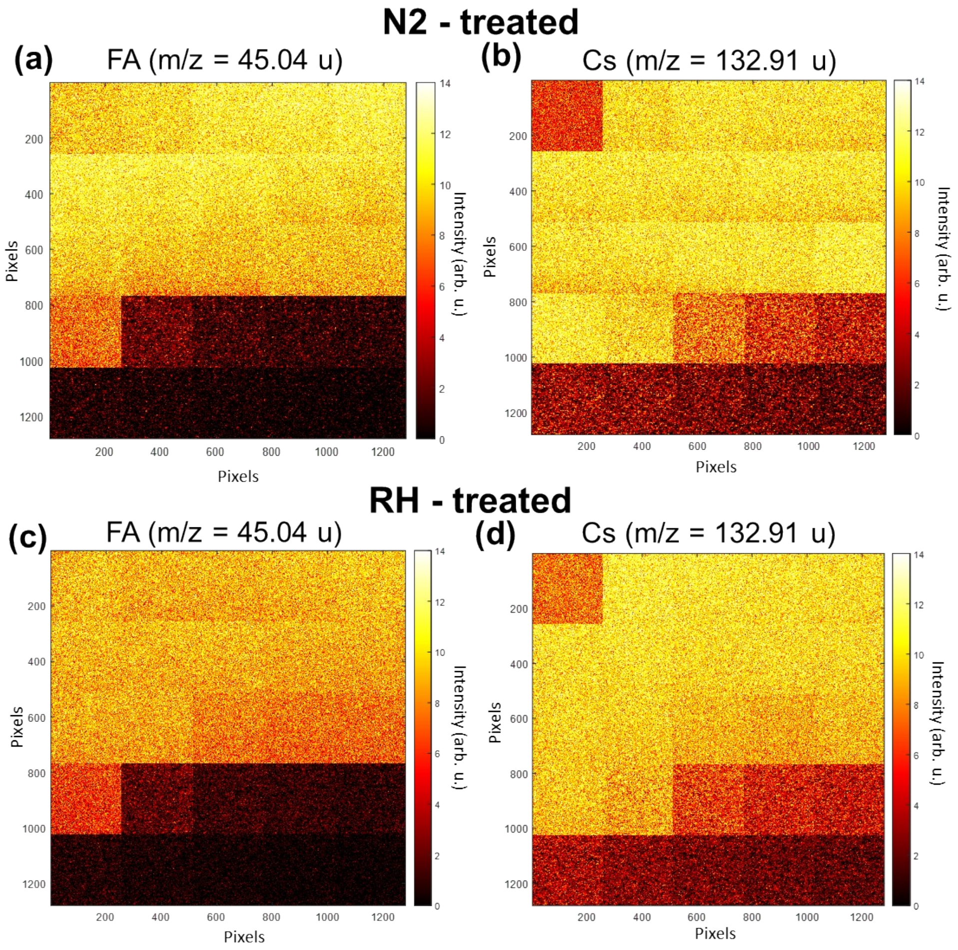

Supplementary Figure 6*:* 100x100 micron depth profiling snapshots of time-of- flight secondary ion mass spectroscopy (ToF-SIMS) for cesium and formamidinium data obtained from sequentially evaporated films annealed in nitrogen (0%RH) and 35%R These figures show the layer-by-layer images for the given ions. The first layer is in the upper left and sequential layers are arranged left to right and top to bottom H.

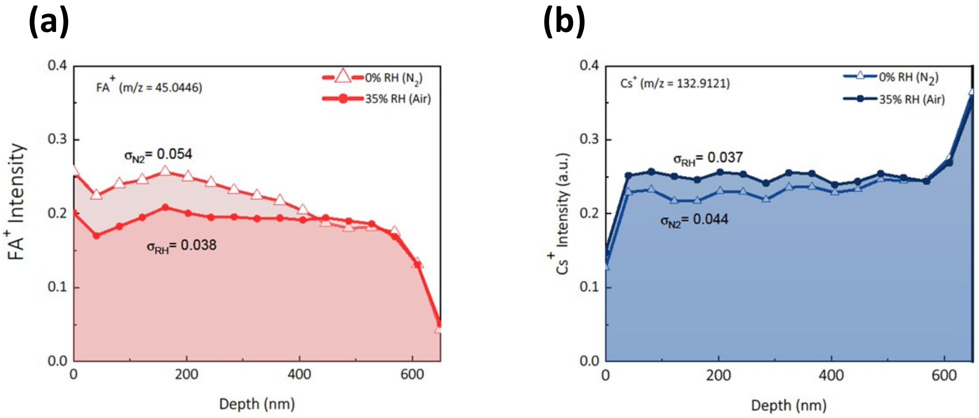

Supplementary Figure 7: 2D plots of point-to-point normalised TOF SIMS signal data along with the standard deviation for a) formamidinium and b) cesium ion signals for sequentially perovskite annealed under 0%RH (in nitrogen) and 35%RH (in air) respectively.

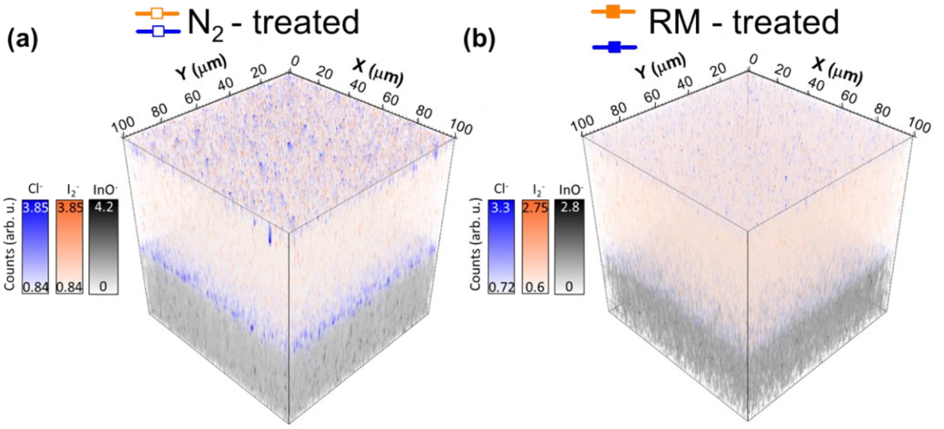

Supplementary Figure 8: 3D plots TOF SIMS signals for iodine and chloride ions for sequentially evaporated perovskite layer annealed under a)0% RH (in nitrogen) and b) 35% RH (in air) respectively

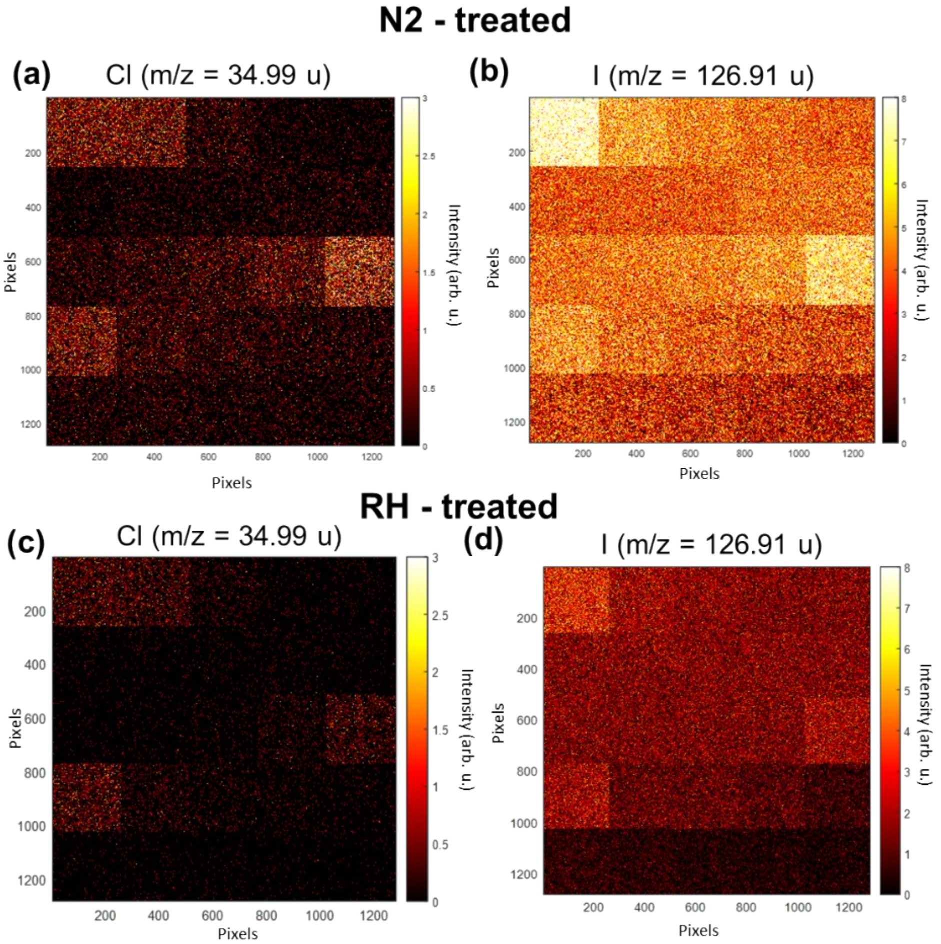

Supplementary Figure 9: 100x100 micron depth profiling snapshots of time-of- flight secondary ion mass spectroscopy (ToF-SIMS) for chloride and iodide data obtained from sequentially evaporated films annealed in nitrogen (0%RH) and 35%RH These figures show the layer by layer images for the given ions. The first layer is in the upper left and sequential layers are arranged left to right and top to bottom.

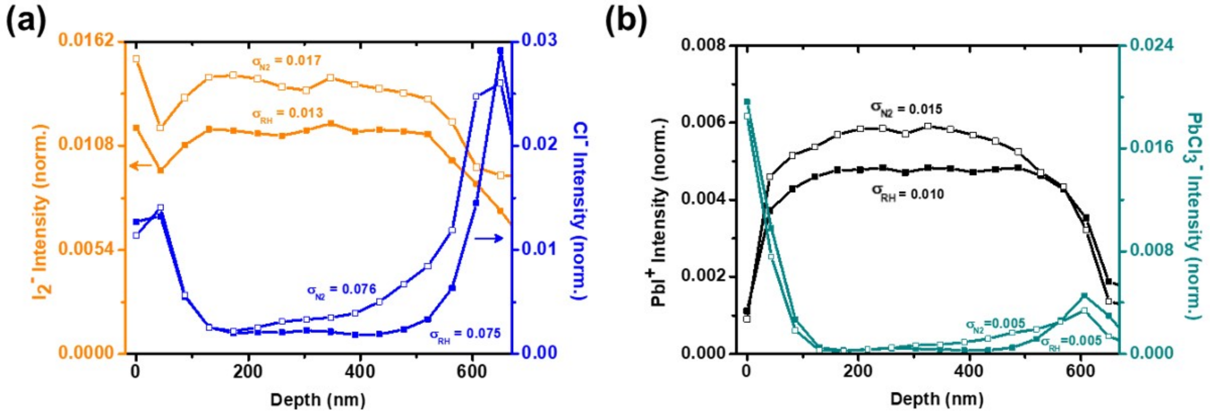

Supplementary Figure 10: a) ToF-SIMS data for iodide and chloride signals through the bulk of the film b) ToF SIMS data for lead iodide and lead chloride signals through the bulk of the film.

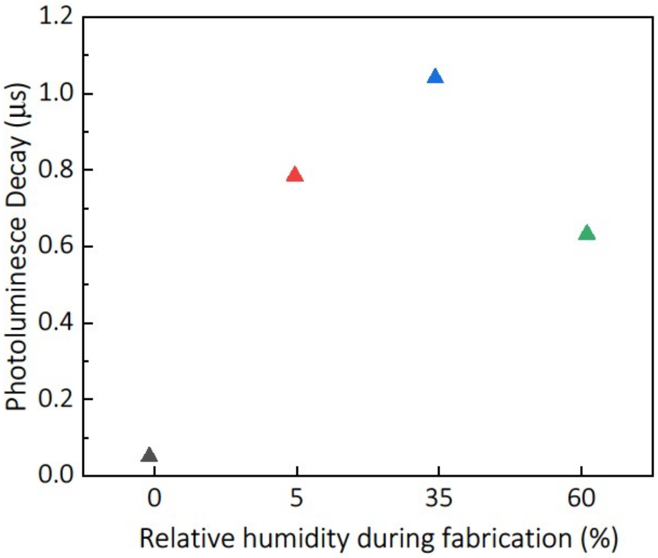

Supplementary Figure 11: PL decay lifetimes (microseconds) obtained from a stretched exponential fit of the TRPL data.

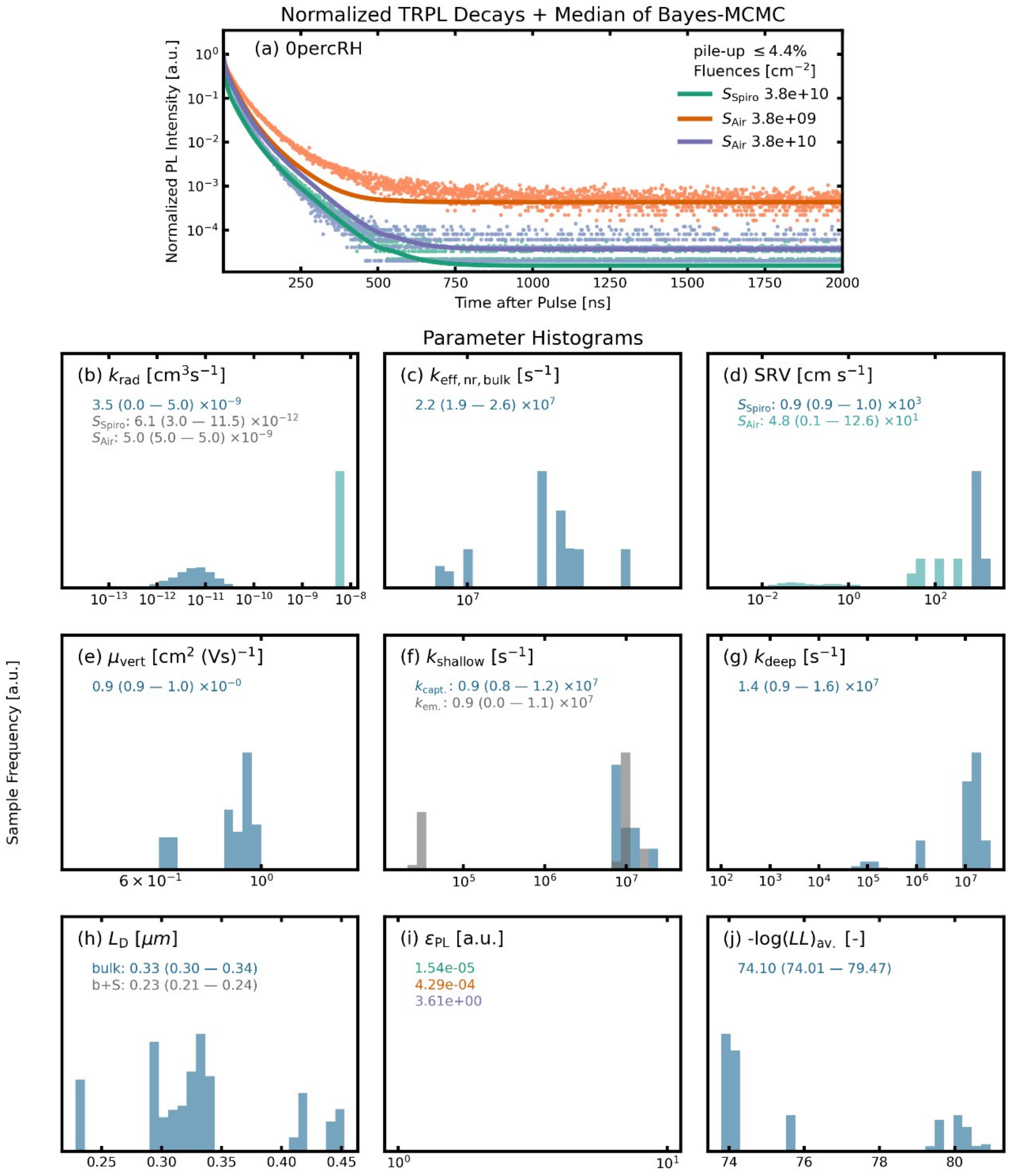

Supplementary Figure 12 The TRPL of the 0%RH sample is shown. The experimental TRPL and median of the last 3000 samples of 10 MCMC chains are shown side-by-side. Both are normalized to the value at t = 0 ns. (b)-(j) shows the normalized sampling frequenciess for all physical parameters used in this modesl: k_{rad} (radiative recombination rate), $k_{eff,nr,bulk}$ (effective, non-radiative bulk recombination rate), SRV (surface recombination velocities), μ_{vert} (vertical, ambipolar mobility), $k_{capt.}$ and $k_{em.}$ (capture and emission of electrons into and from a shallow defect state), k_{deep} (non-radiative recombination rate via a deep defect), L_D (diffusion length), -log(LL)$_{av}$ (average log-likelihood for the dataset), ε_{PL} (instrument error on the PL).

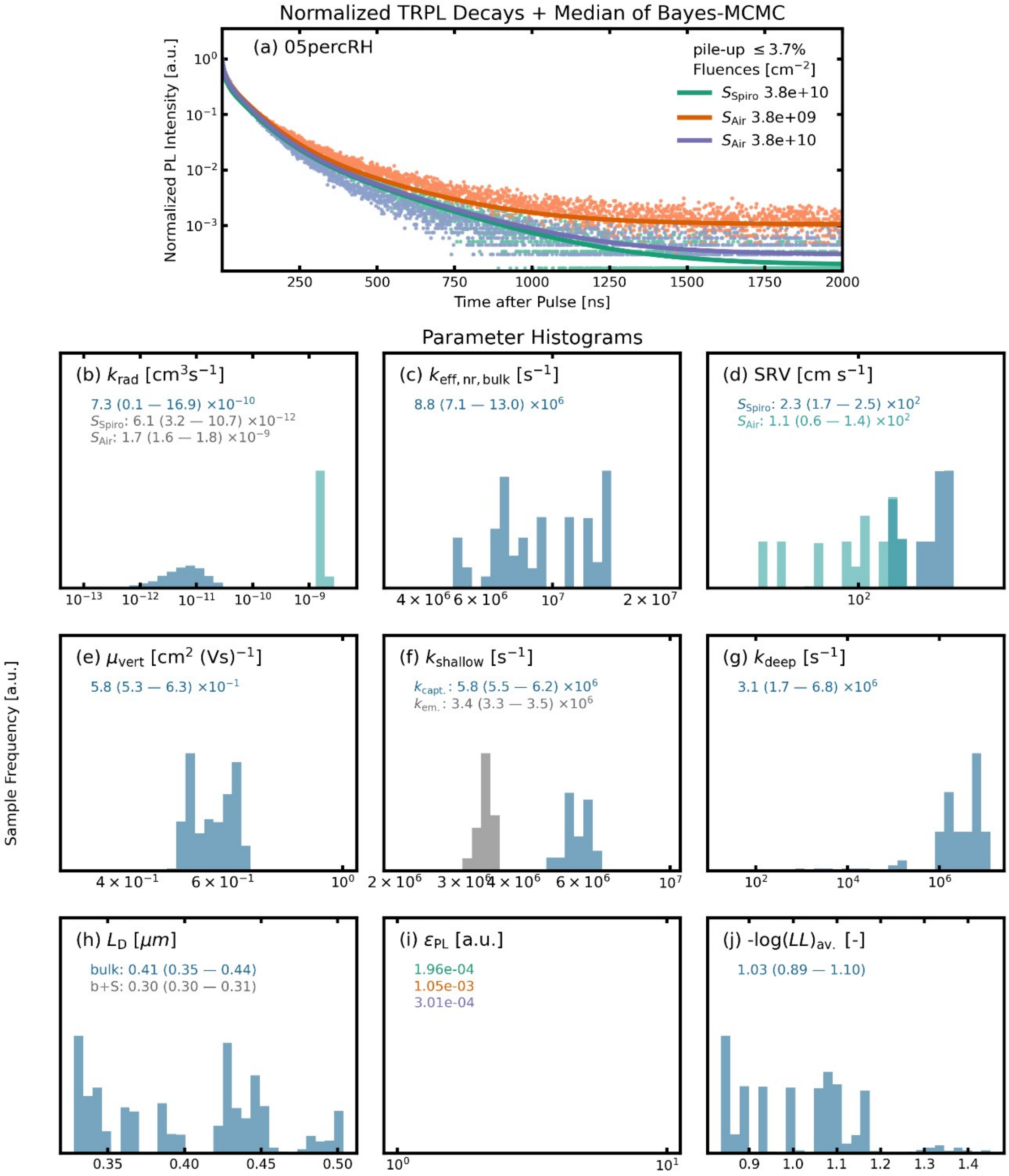

Supplementary Figure 13 The TRPL of the 5%RH sample is shown. The experimental TRPL and median of the last 3000 samples of 10 MCMC chains are shown side-by-side. Both are normalized to the value at t = 0 ns. (b)-(j) shows the normalized sampling frequencies for all physical parameters used in this model: k_{rad} (radiative recombination rate), $k_{eff,nr,bulk}$ (effective, non-radiative bulk recombination rate), SRV (surface recombination velocities), μ_{vert} (vertical, ambipolar mobility), $k_{capt.}$ and $k_{em.}$ (capture and emission of electrons into and from a shallow defect state), k_{deep} (non-radiative recombination rate via a deep defect), L_D (diffusion length), -log(LL)$_{av}$ (average log-likelihood for the dataset), ε_{PL} (instrument error on the PL).

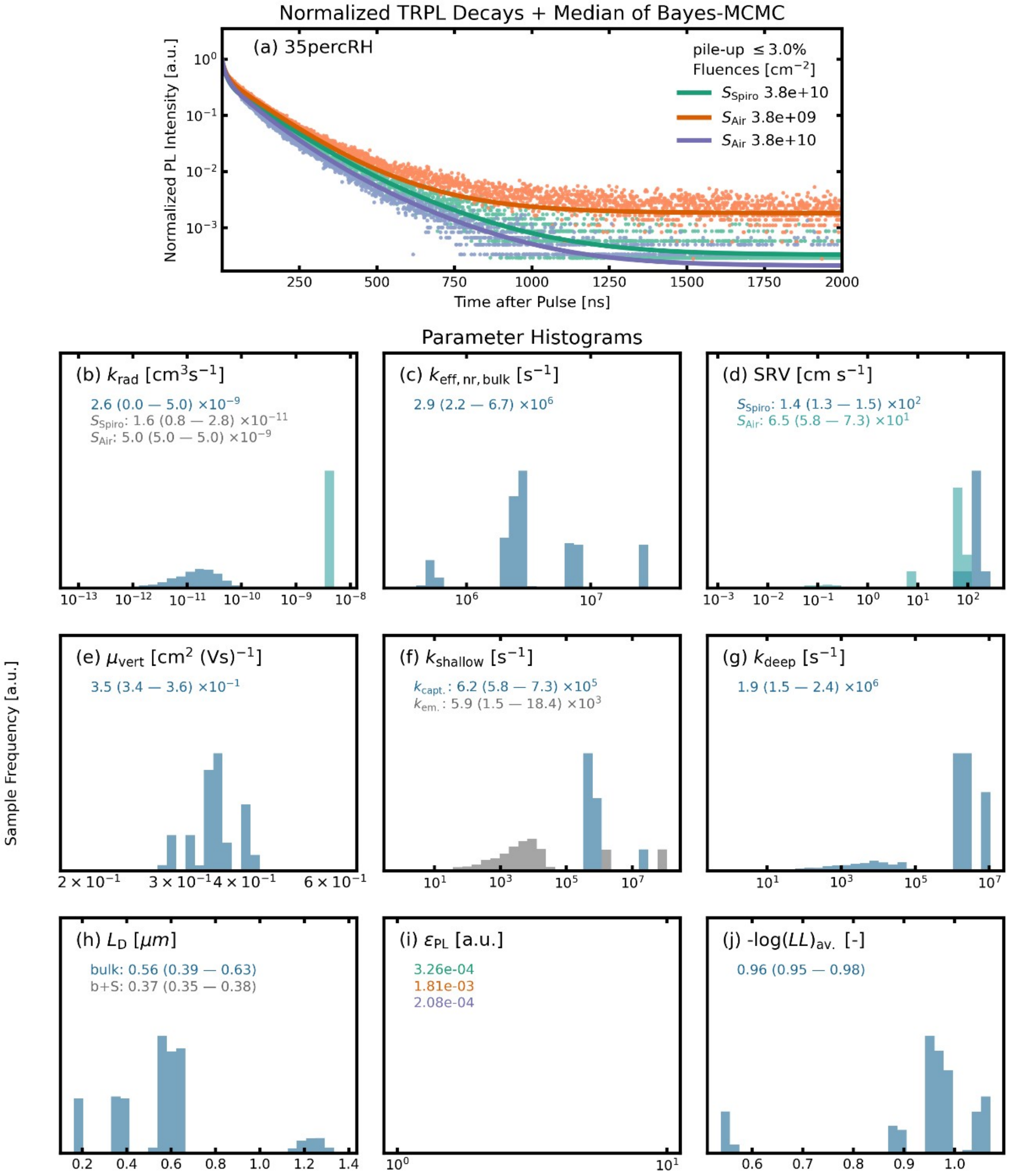

Supplementary Figure 14 The TRPL of the 35%RH sample is shown. The experimental TRPL and median of the last 3000 samples of 10 MCMC chains are shown side-by-side. Both are normalized to the value at t = 0 ns. (b)-(j) shows the normalized sampling frequencies for all physical parameters used in this model: k_{rad} (radiative recombination rate), $k_{eff,nr,bulk}$ (effective, non-radiative bulk recombination rate), SRV (surface recombination velocities), μ_{vert} (vertical, ambipolar mobility), $k_{capt.}$ and $k_{em.}$ (capture and emission of electrons into and from a shallow defect state), k_{deep} (non-radiative recombination rate via a deep defect), L_D (diffusion length), -log(LL)$_{av}$ (average log-likelihood for the dataset), ε_{PL} (instrument error on the PL).

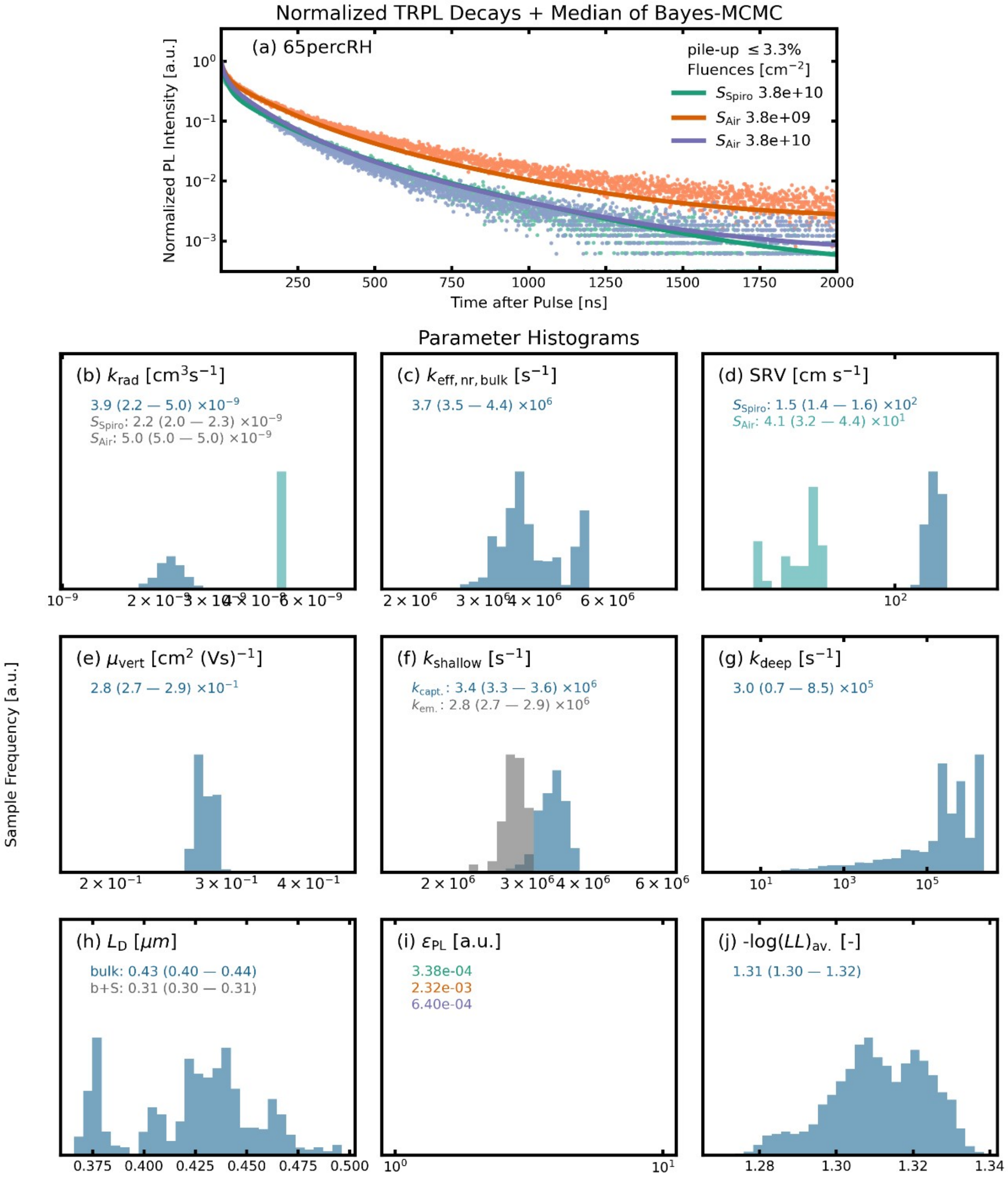

Supplementary Figure 15 The TRPL of the 65%RH sample is shown. The experimental TRPL and median of the last 3000 samples of 10 MCMC chains are shown side-by-side. Both are normalized to the value at t = 0 ns. (b)-(j) shows the normalized sampling frequencies for all physical parameters used in this model: k_{rad} (radiative recombination rate), $k_{eff,nr,bulk}$ (effective, non-radiative bulk recombination rate), SRV (surface recombination velocities), μ_{vert} (vertical, ambipolar mobility), $k_{capt.}$ and $k_{em.}$ (capture and emission of electrons into and from a shallow defect state), k_{deep} (non-radiative recombination rate via a deep defect), L_D (diffusion length), $-\log(LL)_{av}$ (average log-likelihood for the dataset), ε_{PL} (instrument error on the PL).

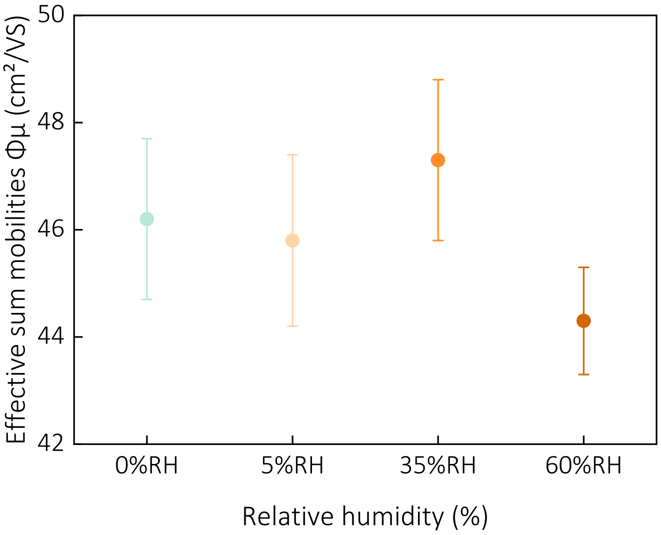

Supplementary Figure 16: THz electron-hole sum mobilities obtained from OPTPs measurements.

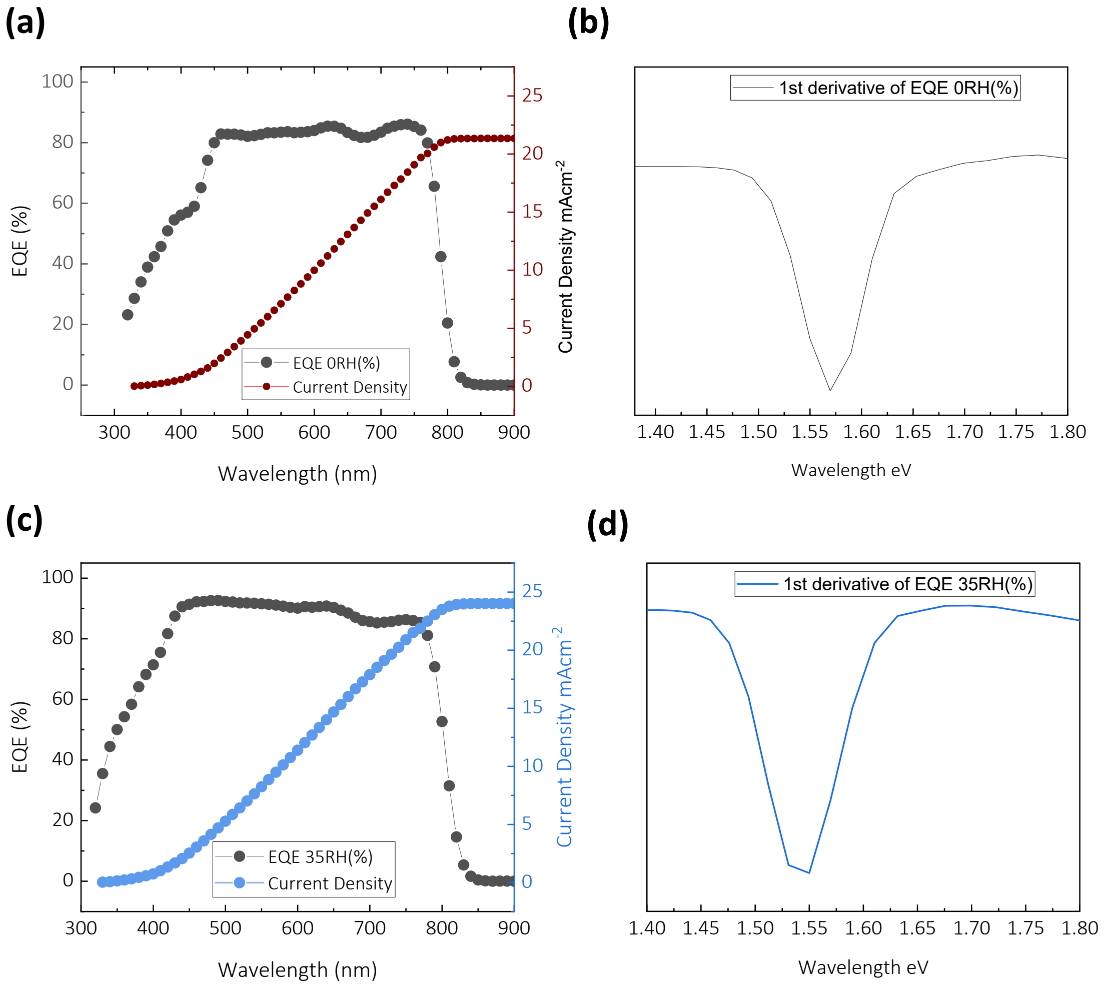

Supplementary Figure 17: (a-b) EQE and bandgap from EQE for fully vacuum processed perovskite solar cell under 0RH(%) conditions shown.(c-d) EQE and bandgap from EQE for fully vacuum processed perovskite solar cell under 35RH(%) conditions shown.

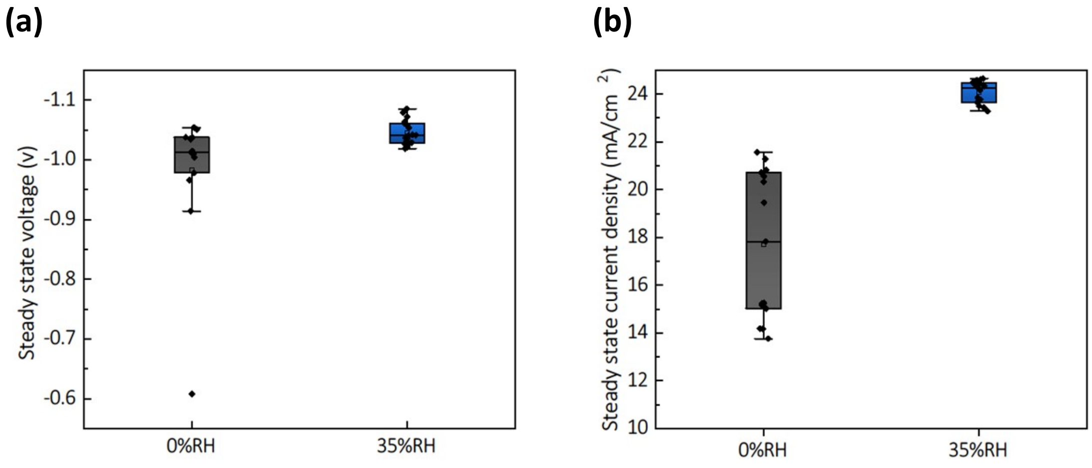

Supplementary Figure 18: A) steady-state open circuit voltage and b) steady-state current density.

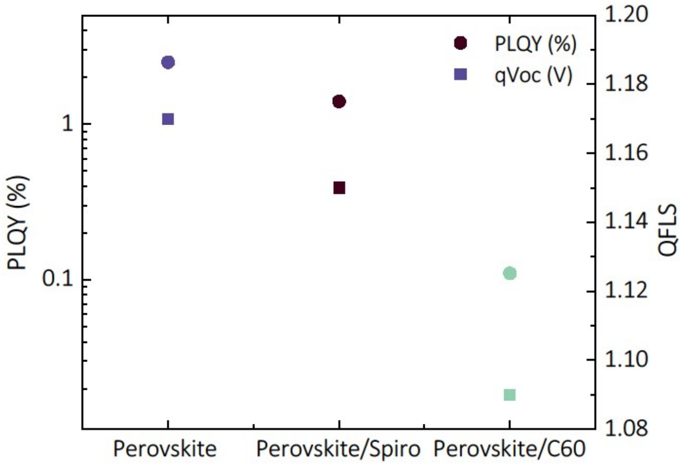

Supplementary Figure 19: Quantification of losses incurred from charge transport layers obtained via performing PLQY with a 532nm laser. The layers are evaporated on z cut quartz substrates.

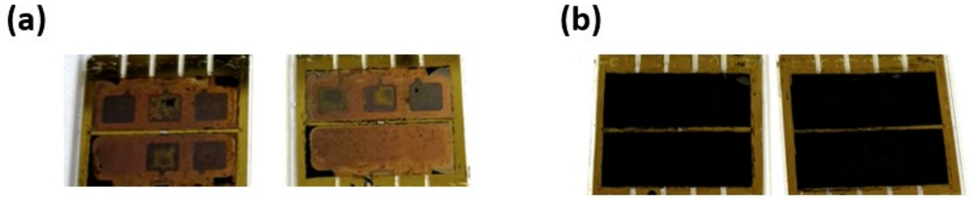

Supplementary Figure 20: Images of pair of PSCs post 200 hours of accelerated ageing under ISOS-L-2 equivalent. (85°C, 0.76 suns illumination, open circuit condition, without UV filter) fabricated under a) 0%RH and b) 35%RH respectively.

References

1. K. B. Lohmann, S. G. Motti, R. D. J. Oliver, A. J. Ramadan, H. C. Sansom, Q. Yuan, K. A. Elmestekawy, J. B. Patel, J. M. Ball, L. M. Herz, H. J. Snaith and M. B. Johnston, *ACS Energy Letters*, 2022, **7**, 1903-1911.
2. T. G. Dane, Github https://github.com/tgdane/pygix).
3. G. Ashiotis, A. Deschildre, Z. Nawaz, J. P. Wright, D. Karkoulis, F. E. Picca and J. Kieffer, *Journal of applied crystallography*, 2015, **48**, 510-519.
4. A. D. Manuel Kober-Czerny, Seongrok Seo, Florine M. Rombach, David P. McMeekin, Heon Jin, Henry J. Snaith, *Submitted*, 2024.
5. R. Elliott, *Physical Review*, 1957, **108**, 1384.
6. C. L. Davies, M. R. Filip, J. B. Patel, T. W. Crothers, C. Verdi, A. D. Wright, R. L. Milot, F. Giustino, M. B. Johnston and L. M. Herz, *Nature communications*, 2018, **9**, 293.
7. C. L. Davies, J. Borchert, C. Q. Xia, R. L. Milot, H. Kraus, M. B. Johnston and L. M. Herz, *The journal of physical chemistry letters*, 2018, **9**, 4502-4511.
8. M. Kober-Czerny, S. G. Motti, P. Holzhey, B. Wenger, J. Lim, L. M. Herz and H. J. Snaith, *Advanced Functional Materials*, 2022, **32**, 2203064.